Boosting the Electrocatalytic Oxygen Evolution of Perovskite $LaCo_{1-x}Fe_xO_3$ by Construction of Yolk-Shell Nanostructures and Electronic Modulation

Bian Bao, Yana Liu, Mingzi Sun, Bolong Huang, Yang Hu, Deguang Ji, Pinxian Xi,* and Chun-Hua Yan*

B. Bao, Y. Liu, Dr. Y. Hu, D. Ji, Prof. P. Xi, Prof. C.-H. Yan
State Key Laboratory of Applied Organic Chemistry
Frontiers Science Center for Rare Isotopes
College of Chemistry and Chemical Engineering
Lanzhou University
Lanzhou 730000, China
E-mail: xipx@lzu.edu.cn

M. Sun, Prof. B. Huang
Department of Applied Biology and Chemical Technology
The Hong Kong Polytechnic University
Hung Hom, Kowloon, Hong Kong SAR, China
E-mail: bhuang@polyu.edu.hk

Prof. C.-H. Yan
Beijing National Laboratory for Molecular Sciences
State Key Laboratory of Rare Earth Materials Chemistry and Applications
PKU-HKU Joint Laboratory in Rare Earth Materials and Bioinorganic Chemistry
Peking University
Beijing 100871, China

Keywords: yolk-shell nanostructures, electronic modulations, oxygen evolution reaction, surface reconstruction, zinc–air batteries

Realizing rational design of perovskite oxides with controllable compositions and nanostructures remains a tremendous challenge for developments of efficient electrocatalysts. Herein, we develop a ligand-assisted synthetic strategy to fabricate perovskite

oxides $LaCo_{1-x}Fe_xO_3$ with yolk-shell nanostructures. Benefiting from the unique structural and compositional merits, $LaCo_{0.75}Fe_{0.25}O_3$ exhibits an overpotential of 310 mV at a current density of 10 mA cm^{-2} and long-term stability of 100 h for the oxygen evolution reaction. In situ Raman spectroscopy demonstrates that Fe substitution facilitates the pre-oxidation of Co sites and induces the surface reconstruction into active Co oxyhydroxides at a relatively lower applied potential, guranteeing the excellent catalytic performances. Density functional theory calculations unravel that the appropriate introduction of Fe into perovskite $LaCoO_3$ leads to the improved electroactivity and durability of the catalyst for OER. Fe-3d orbitals show a pinning effect on Co-3d orbitals to maintain the stable valence state of Co sites at the low overpotential of the OER. Furthermore, Zn-air batteries assembled with $LaCo_{0.75}Fe_{0.25}O_3$ displays a high open circuit potential of 1.47 V, superior energy density of 905 Wh kg^{-1} $_{Zn,}$ and excellent stability in a large temperature range. This work supplies novel insights into the future developments of perovskite-based electrocatalysts.

1. Introduction

Ever-growing energy demands and depleting fossil-fuel resources have made the development of sustainable energy storage and conversion technologies a global imperative.[1] Zinc-air batteries (ZABs) with high theoretical energy density, better safety and lower cost are commonly considered as one of the most promising portable devices for energy storage systems.[2–4] A core problem of ZABs development is the exploration of air cathodes that are capable of efficiently catalyzing both oxygen evolution reaction (OER) and oxygen reduction reaction (ORR) for long-term stable operation, but their potential has not been fully realized due to high polarization and short lifetime at the air cathodes.[5] Although precious metal Pt-based or Ir/Ru-based materials demonstrate remarkable catalytic performance for the OER and ORR, their large-scale applications are hindered by their scarcity and high cost.[6] Therefore, considerable efforts have been devoted to designing nonprecious metal-based electrocatalysts with low-cost, earth-abundance, and high catalytic activity.[7,8]

Owing to their excellent compositional and structural flexibility, tunable electronic structure and high intrinsic activity, perovskite oxides (ABO_3), particularly $LaCoO_3$, have been widely studied and demonstrate great potential as electrocatalysts for energy storage and conversion.[9,10] With a general formula of ABO_3, B-site cations form the corner-sharing BO_6 octahedra with O anions and A-site cations occupy the 12-fold coordinated sites within the cavity of neighboring octahedra.[11] Nevertheless, the electrocatalytic performance of bulk $LaCoO_3$ without further modification is far below expectation, thus inspiring us to develop

effective strategies for structure optimization. Tuning electronic structures of perovskite oxides by cation doping is deemed as an important method to strengthen their electrocatalytic activity.[12,13] As the e_g electron filling of perovskite approaches 1, higher catalytic activity can be obtained.[14] Meanwhile, $LaCoO_3$ with optimal electronic configuration can enhance the covalency of the bonding between Co-3d and O-2p to lower the adsorption energies of oxygen intermediates.[15] In addition, the better electrical conductivity of electrocatalysts can promote electron transfer at the interface during OER process, which is beneficial for enhancing the catalytic performance. Apart from regulating the composition, the delicate engineering of favorable structures for the perovskite materials is also of significant importance to enhance their electrocatalytic performance.

Fine micro/nanostructures engineering with subtle morphologies represents an effective strategy to enhance the catalytic performance of the materials through exposing abundant electrochemically active sites and facilitating mass diffusion efficiency. In particular, yolk-shell nanostructures (YSNs) with well-defined interior cavities and functional exterior shells have attracted much attention for applications in catalysis, lithium-ion batteries, nanoreactors and energy storage and conversion.[16] To be specific, YSNs hold readily accessible and adjustable porous shells, which enables the control of the diffusion rates for reactants to improve the selectivity of catalytic reactions. Besides, YSNs that contain a large hollow space between the core and shell provide a homogeneous reaction environment for heterogeneous catalysis. Moreover, YSNs with a core@void@shell configuration possess shorten the diffusion pathway of charges and high surface-area-to-volume ratios, which promote reaction dynamics. However, the current methods are mostly based on the conventional sol-gel method and the obtained perovskite materials usually have large sizes and few morphological features, resulting in limited catalytic activity and thus posing a major challenge to practical application. More importanly, due to the lack of suitable methods to simultaneously satisfy the morphology uniformity and structural integrity of different metal components in the synthesis process, it is difficult to prepare multicomponent perovskite oxides with yolk-shell nanostructures. Therefore, it is still challenging to design perovskite oxides with controllable compositions and nanostructures.

Herein, we develop a general ligand-assisted strategy for the efficient synthesis of a series of perovskite oxides $LaCo_{1-x}Fe_xO_3$ YSNs (x = 0.00, 0.10, 0.25, 0.50, 0.75 and 1.00) with precisely tuable molar ratios of Co and Fe. The strategy involves the preparation of precursors La-M-BTC solid microspheres through solvothermal reactions and subsequent thermal annealing processes in air. The obtained YSNs is constructed by the protective shell and possesses large

hollow space between the core and shell. Remarkably, the optimized $LaCo_{0.75}Fe_{0.25}O_3$ YSNs exhibits excellent electrocatalytic activity with an extremely low overpotential of 310 mV at 10 mA cm^{-2}, outperforming many reported Co/Fe-rich perovskite oxides. Additionally, $LaCo_{0.75}Fe_{0.25}O_3$ YSNs displays robust operation durability with negligible activity loss under alkaline OER conditions for over 100 h. Combined with *operando* spectroscopic characterizations and theoretical calculations, the appropriate doping of Fe into perovskite $LaCoO_3$ optimizes the electronic structures in $LaCo_{0.75}Fe_{0.25}O_3$ through the protection of valence states in Co sites and the activation of surface O sites. With the electronic modulations, the low overpotential and high durability for OER are achieved. As a proof-of-concept application, a rechargeable ZAB assembled with the $LaCo_{0.75}Fe_{0.25}O_3$ YSNs as the cathode exhibits a high open circuit potential of 1.47 V, an outstanding energy density of 905 Wh kg^{-1}_{Zn}, supporting the high potential for practical applications in a wide temperature window.

2. Results and Discussion

2.1. Synthesis and structural characterization

Perovskite oxides with unique yolk-shell structures were obtained by exploring and studying the preparation conditions (Figure S1−S6, Supporting Information). The overall strategy for the formation of $LaCo_{1-x}Fe_xO_3$ YSNs was illustrated in Figure S1, using $LaCoO_3$ as an example. The uniform La-Co-BTC solid microspheres as the precursor were first prepared by a solvothermal reaction (Figure S7, Supporting Information). Subsequently, the La-Co-BTC solid microspheres could be easily converted to $LaCoO_3$ YSNs by a simple nonequilibrium heat treatment process. The formation of the $LaCoO_3$ YSNs was mainly based on the heterogeneous contraction induced by nonequilibrium heat treatment during the thermal decomposition of La-Co-BTC solid microspheres.[17] The morphological evolution and crystallization process at different periods of thermal treatment were characterized by transmission electron microscopy (TEM), powder X-ray diffraction (XRD) and Raman spectroscopy (Figure S8 and S9, Supporting Information). At the initial stage of calcination, there exists a large temperature gradient (ΔT) along the radial direction (stage I), resulting in the rapid formation of a $LaCoO_3$ shell at the surface of the La-Co-BTC microspheres. Meanwhile, several weak diffraction peaks appeared in the corresponding XRD pattern can be indexed to the crystal planes of $LaCoO_3$. Two forces of opposite directions act on the interface between the $LaCoO_3$ shell and the La-Co-BTC core. The contraction force (F_c) caused by oxidative degradation of the organic species promotes the inward shrinkage of the La-Co-BTC core, while another adhesion force (F_a) from the relatively rigid shell restrains the inward contraction of the precursor core. When F_c is

dominant (stage II), the further inward shrinkage leads to the detachment of the core from the preformed outer shell, thus producing unique yolk-shell structure, as confirmed by TEM images. The increase of diffraction peak intensity in XRD and the appearance of characteristic peaks in Raman spectrum also indicate gradually increased crystallinity with the increase of temperature. Importantly, the present synthetic approach is highly versatile and can be extended to the synthesis of other perovskite oxides YSNs with accurately controlled composition (Figure S10−12, Supporting Information).

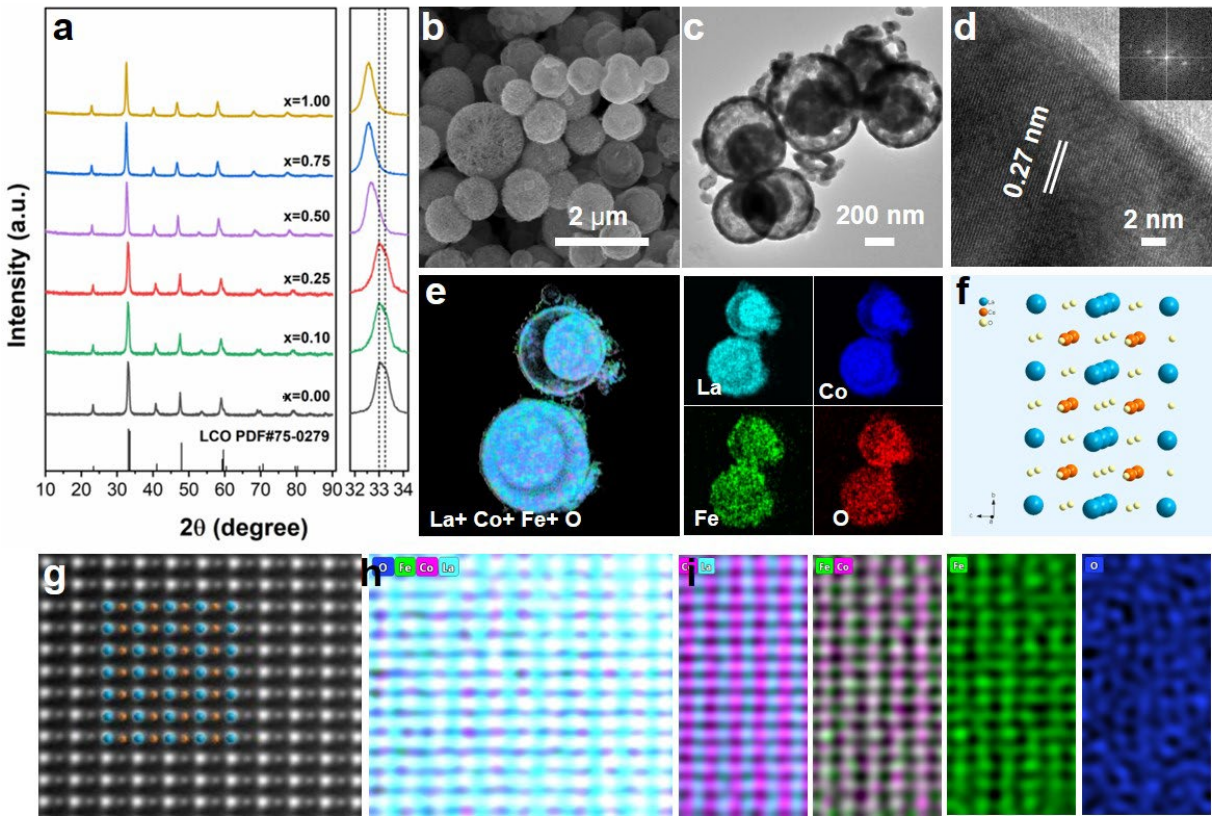

Figure 1. a) XRD patterns of $LaCo_{1-x}Fe_xO_3$ (x = 0.00, 0.10, 0.25, 0.50, 0.75 and 1.00). $LaCo_{0.75}Fe_{0.25}O_3$: b) SEM image. c) TEM image. d) HRTEM image (inset: Corresponding FFT pattern). e) Elemental mappings. f) The atomic structure diagram. g−i) Atomic resolution HAADF-STEM image and corresponding EDS elemental mapping images.

The crystal structures of the $LaCo_{1-x}Fe_xO_3$ were initially characterized by XRD. As displayed in Figure 1a, the diffraction peaks of the as-prepared $LaCoO_3$ match with that of the standard cubic perovskite oxides with *Pm*-3*m* space group (JCPDS No. 75-0279). $LaCo_{1-x}Fe_xO_3$ oxides with different Fe substitution amounts remain in the cubic perovskite structure without the appearance of any impurity phase. Furthermore, the main diffraction peak exhibits a shift to a lower angle relative to those for $LaCoO_3$ with increasing Fe substitution amount. This shift can be ascribed to the lattice expansion induced by the different ionic radius of Co and Fe cations,

implying the success of Fe atom doping into the $LaCoO_3$ lattice. The contents of Co and Fe elements in $LaCo_{1-x}Fe_xO_3$ YSNs are determined by the energy dispersive X-ray spectroscopy (EDS) and inductively coupled plasma optical emission spectroscopy (ICP-OES), which show that the actual ratio of Fe/(Co + Fe) in the product is almost the same with the feeding ratio of metal precursors (Table S1, Supporting Information). As displayed by scanning electron microscope (SEM) images (Figure S13, Supporting Information), there are significant differences in the morphology and particle size of undoped and Fe-doped $LaCoO_3$, which is consistent with their differences in the specific surface area measured by Brunauer-Emmet-Teller (BET) (Figure S14 and Table S2, Supporting Information). Moreover, the high-resolution transmission electron microscopy (HRTEM) images of as-synthesized $LaCoO_3$ and $LaCo_{0.75}Fe_{0.25}O_3$ reveal that their surfaces and bulk are highly crystalline (Figures 1d and S10d, Supporting Information). The interplane distances of 0.27 nm correspond to the (110) crystal plane of the cubic perovskite structure, which was further verified by the Fast Fourier Transformation (FFT) patterns. In addition, the elemental mapping images demonstrate the homogeneous distribution of La, Co, Fe, and O in the entire architecture, this result indicates the successful incorporation of Fe atoms (Figure 1e). To further disclose the position of Fe atoms and the lattice structure of $LaCo_{0.75}Fe_{0.25}O_3$ YSNs, the atomic-resolution high-angle annular dark field aberration-corrected scanning transmission electron microscopy (HAADF-STEM) image was directly performed to analyze the atom arrangements (Figure 1f,g). As can be seen that all the atoms are well arranged and can be distinguished by their obvious difference in luminance, with the brightest and slightly darker spots identified as La and Co atoms, respectively. In addition, the corresponding EDS atomic elemental mappings also intuitively observe the Fe atom position (Figure 1h,i). Therefore, we can conclude that Fe doping can only substitute Co sites due to the similar radius between Fe and Co atoms and the absence of interstitial atoms in the images. Thus, all the above results verified the successful production of $LaCo_{0.75}Fe_{0.25}O_3$ YSNs.

2.2. Electronic Structure

The OER electrocatalytic activities of the synthesized $LaCo_{1-x}Fe_xO_3$ YSNs were evaluated by linear sweep voltammetry (LSV) in 1.0 M KOH electrolyte. As shown in Figure S15 in the Supporting Information, the OER activity was significantly improved by the incorporation of Fe into the lattice of $LaCoO_3$, and the maximum enhancement effect was achieved when the value of x in $LaCo_{1-x}Fe_xO_3$ was 0.25. Among the investigated Fe-doped $LaCoO_3$ catalysts,

$LaCo_{0.75}Fe_{0.25}O_3$ exhibited the highest OER activity and was selected for further study together with its opposite $LaCo_{0.25}Fe_{0.75}O_3$.

To explore the change in electronic structures and coordination environments of the materials, X-ray photoelectron spectroscopy (XPS) and X-ray absorption spectroscopy (XAS) were carried out. The XPS spectra of La 3d exhibits two peaks of La $3d_{3/2}$ (850.8 and 854.6 eV) and La $3d_{5/2}$ (834.0 and 837.7 eV), demonstrating the presence of La^{3+} in $LaCo_{1-x}Fe_xO_3$ (Figure S16a, Supporting Information). Figure S16b shows the XPS spectra of Co 2p, the main peaks at 779.8 and 781.1 eV are attributed to Co^{3+} $2p_{3/2}$ and Co^{2+} $2p_{3/2}$, respectively, demonstrating the coexistence of Co^{3+} and Co^{2+} in samples. There is almost no energy shift of $LaCo_{0.75}Fe_{0.25}O_3$ and $LaCo_{0.25}Fe_{0.75}O_3$ relative to $LaCoO_3$, indicating that the valence states of Co cations remain almost constant in three samples.[18] Meanwhile, the O 1s spectra can be deconvoluted into four characteristic peaks of lattice oxygen species (529.0 eV for O1), defect sites with low oxygen coordination (529.5 eV for O2), hydroxyl groups or surface-adsorbed oxygen (531.5 eV for O3), and adsorbed molecular water (533.4 eV for O4) (Figure S17, Supporting Information). The ratio of O2/O1 is considered an important parameter to reflect the relative concentration of surface oxygen vacancies.[19] Based on the deconvolution results, $LaCo_{0.75}Fe_{0.25}O_3$ (4.684 %) and $LaCo_{0.25}Fe_{0.75}O_3$ (1.232 %) shows the highest surface oxygen vacancy concentration than $LaCoO_3$ (1.078 %), indicating that there are more oxygen vacancies on the surface after Fe substitution (Table S3, Supporting Information). Although abundant oxygen vacancies have been generated on the surface, it is worth noting that the crystal structure remains well in the bulk phase, which is because the calculated oxygen vacancy is mainly distributed on the surface of the materials.

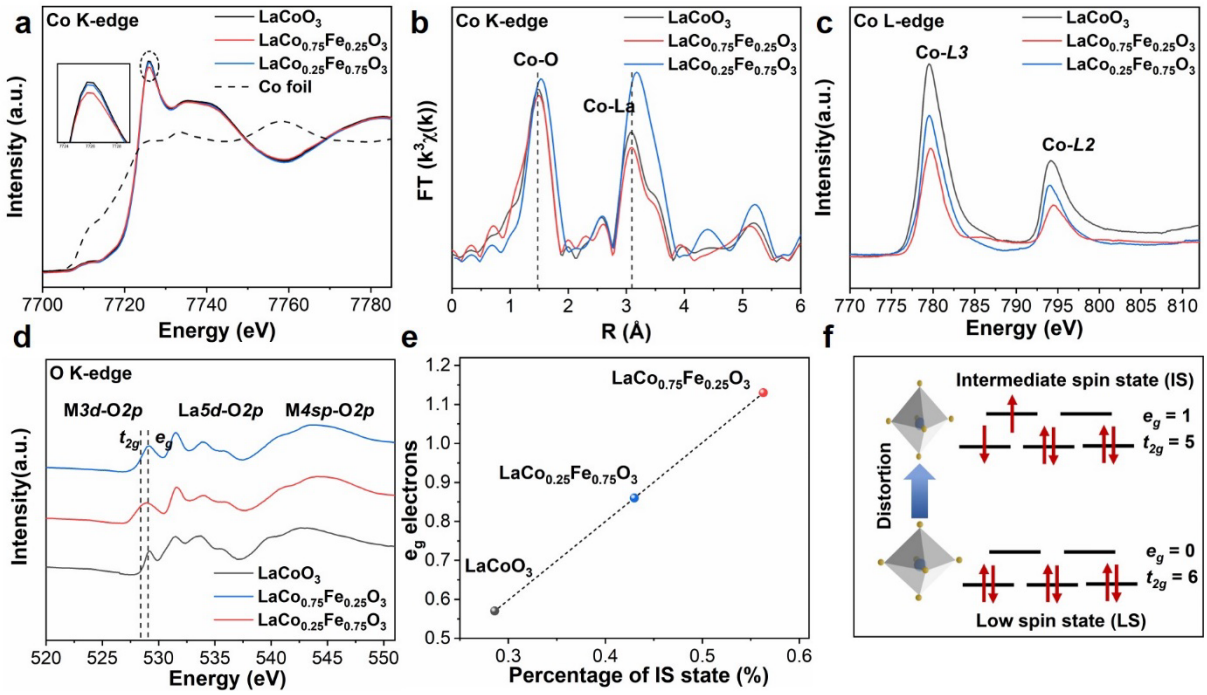

Figure 2. a) Co K-edge XANES spectra of $LaCoO_3$, $LaCo_{0.75}Fe_{0.25}O_3$ and $LaCo_{0.25}Fe_{0.75}O_3$. b) Co K-edge FT-EXAFS spectra in *R* space. c) Co L-edge. d) O K-edge. e) The corresponding e_g filling. f) Schematic illustration of the transition of electrons from t_{2g} to e_g orbital and the evolution of IS state.

As shown in Co K-edge X-ray absorption near edge spectroscopy (XANES) from Figure 2a, with the substitution amounts of Fe increase, there is almost no energy shift of $LaCo_{0.75}Fe_{0.25}O_3$ and $LaCo_{0.25}Fe_{0.75}O_3$ compared with $LaCoO_3$, which agrees well with the XPS results that no obvious change in the valence state of Co after Fe substitution. The intensity of the main absorption peak over the $LaCo_{0.75}Fe_{0.25}O_3$ is slightly lower than that of $LaCoO_3$ and $LaCo_{0.25}Fe_{0.75}O_3$, indicating a higher degree of lattice disorder and less unoccupied electronic states.[20] Although no obvious energy shift of the Co K-edge XANES results, the K-edge energies of Fe in $LaCo_{0.75}Fe_{0.25}O_3$ is significantly shifted to low energy compared to $LaCo_{0.25}Fe_{0.75}O_3$, indicating a decrease in the valence state of Fe (Figure S18a, Supporting Information). This phenomenon could be rationalized by the creation of more oxygen vacancies. Extended X-ray absorption fine structure (EXAFS) is employed to further study the local chemical environment of Co and Fe sites. As observed in the Fourier transformed (FT) EXAFS spectra from Figure 2b, there are two distinct peaks at about 1.5 and 3.2 Å assigned to the radial distance of Co atom to the closest neighboring O atom (Co−O) and La atom (Co-La), respectively.

The radial distance between Co and O atom in $LaCo_{0.75}Fe_{0.25}O_3$ and $LaCo_{0.25}Fe_{0.75}O_3$ is slightly longer than $LaCoO_3$, among which $LaCo_{0.25}Fe_{0.75}O_3$ possesses the largest Co−O bond length and smallest Fe−O bond length (Figure S18b, Supporting Information). These results suggest that Fe substitution induces a distortion in the perovskite structure. In addition, the peak intensities of the Co-La are significantly lower for $LaCo_{0.75}Fe_{0.25}O_3$ and $LaCo_{0.25}Fe_{0.75}O_3$, indicating the more local disorder for the second shell in comparison to that for $LaCoO_3$.[21] Moreover, X-ray absorption near-edge structure (XANES) of Co L-edge and O K-edge provides a subtle change in the electronic structure. As shown in Figure 3c, the Co L-edge spectra is divided into L_2-edge and L_3-edge peaks owing to the spin-orbital coupling, where the absorption intensity of the L_3-edge peak directly reflects the unoccupied states of cobalt e_g orbitals.[22] Notably, compared with $LaCoO_3$, the obvious reduction in the intensity of the Co L_3-edge peaks for the $LaCo_{0.75}Fe_{0.25}O_3$ and $LaCo_{0.25}Fe_{0.75}O_3$ suggests that partial e_g orbitals are filled, forming the transition from a low spin state (LS) to a higher spin state. As shown in Figure 3d, three different regions can be identified in the O K-edge spectra, where the first one (regions I) is ascribed to the hybridization between O 2p state and Co 3d state, and the rest regions (regions II and III) are assigned to the hybridization of O 2p with La 5d and Co 4sp states, respectively.[23]

With the introduction of Fe, the entire spectrum broadening increases and is more evident in the lower energy regions. In addition, the pre-edge feature (regions I) is related to the filling of the hybridized O 2p and Co 3d states.[24] The pre-peak of O K-edge slightly shifts toward lower energy and shows an obvious reduction in the intensity, especially for $LaCo_{0.75}Fe_{0.25}O_3$. Such a change was ascribed to the electronic redistribution between e_g and t_{2g} levels caused by electrons transition. Thus, Fe substitution contributes to the emergence of a higher spin state for the Co^{3+} ion.[25] To further verify the spin configurations of Co ions for all the samples, the temperature-dependent magnetizations were measured with an external magnetic field of H =1 kOe under field-cooling procedures.[26] The effective magnetic moment μ_{eff} can be calculated through $\mu_{eff} = \sqrt{8C}\mu_B$ by fitting the curves of inverse susceptibilities and temperature (Figure S19, Supporting Information). The μ_{eff} for three samples is estimated to be 2.62 μ_B, 3.68 μ_B and 3.22 μ_B, which corresponds to e_g filling is about 0.57, 1.13 and 0.86, respectively (Figure 3e and Table S4, Supporting Information)). The results suggest that Fe doping can tune the e_g filling and the optimal configuration of 1.12 is obtained when the substitution of Fe is 0.25. Figure 3f illustrates that the crystal lattice distortion and the electronic configuration transformation are induced by Fe substitution. Therefore, such an electronic configuration ($t_{2g}^5 e_g^1$) will favor the improvement of electrocatalytic performance.

2.3. Density Functional Calculations

To further understand the improved OER performances, we have applied theoretical calculations through the DFT calculations. Different concentration of Fe leads to varied electroactivity on the surface of the catalysts (Figure 3a). $LaCo_{0.75}Fe_{0.25}O_3$ has shown the electron-rich surface with high electroactivity, where the bonding orbitals are mostly dominated by the surface Co sites. Meanwhile, it is noted that the minor introduction has induced evident lattice distortion, leading to activation of the surface O sites to improve the site-to-site electron transfer. For the $LaCo_{0.25}Fe_{0.75}O_3$, it has exhibited much weaker electroactivity since the anti-bonding orbitals become the main contributions on the surface (Figure 3b). Notably, the high Fe concentration also leads to lower lattice distortions. In comparison, the $LaCoO_3$ has shown an improved electroactivity, where the Co and O sites show limited contributions to the bonding orbitals (Figure 3c). The projected partial density of states (PDOS) further reveal the electronic structures of different electrocatalysts. For $LaCo_{0.75}Fe_{0.25}O_3$, we notice that Co-3d orbitals demonstrate high electron density near the Fermi level (E_F), which supplies the high electron transfer as the active sites for OER (Figure 3d). Meanwhile, Co-3d locate in the center of the e_g–t_{2g} splitting of Fe-3d orbitals, which offers the protected environment to achieve a robust valence state of Co sites. We notice that Fe-3d and Co-3d orbitals have displayed overlapping, which supplies the effective orbital coupling. The overlapping between the La-5d and O-s,p orbitals leads to the stable structure of $LaCo_{0.75}Fe_{0.25}O_3$. As the concentration of Fe increases, we notice that Co-3d orbitals have downshifted, representing the decreased electroactivity in $LaCo_{0.25}Fe_{0.75}O_3$ (Figure 3e). With the improved concentration of Fe, the e_g–t_{2g} splitting of Fe accordingly decreases. Moreover, we notice the overlapping between Co-3d and Fe-3d reduces, leading to weakened site-to-site electron transfer. For the $LaCoO_3$, we notice that Co-3d orbitals show a high electron density near E_F, representing a similar valence state to $LaCo_{0.75}Fe_{0.25}O_3$ (Figure 3f). However, without the protection of Fe sites, the valence change of Co-3d orbitals will lead to the decreased electroactivity and durability of the $LaCoO_3$. For the site-dependent Co sites, we notice that the electron density of Co-3d near E_F is increasing from the bulk to the surface, supporting the higher electroactivity (Figure 3g). In the meantime, the e_g–t_{2g} splitting of Fe-3d has been extended from 1.13 eV in the bulk to 1.65 eV on the surface, which supplies the pinning effect to Co-3d orbitals with effective protection on the valence states (Figure 3h). These electronic structure characterizations confirm that the suitable Fe doping in the perovskite is able to optimize the electronic structures through the stabilization of Co sites. Moreover, the long-term stability is also significantly improved by the introduction of Fe. For the key adsorbates in the OER process, the σ orbitals of O-species demonstrate the nearly linear

correlations (Figure 3i). The corresponding structural configurations reveal that Co is the active site for the efficient intermediate conversions and low overpotential for the OER process.

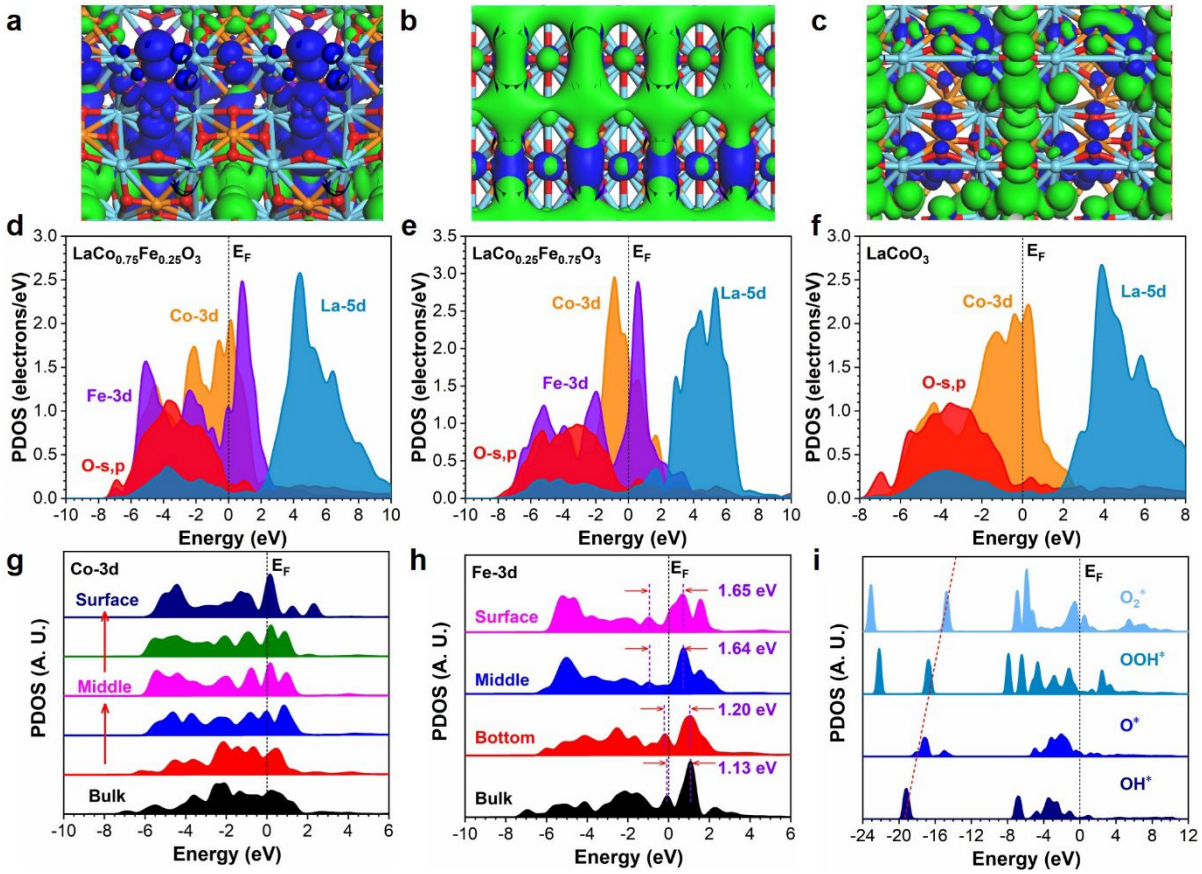

Figure 3. The 3D contour plot of electronic distribution near Fermi level of a) $LaCo_{0.75}Fe_{0.25}O_3$, b) $LaCo_{0.25}Fe_{0.75}O_3$, and c) $LaCoO_3$. Orange balls = Co, purple balls = Fe and red balls = O. Blue isosurface = bonding orbitals and green isosurface = anti-bonding orbitals. The PDOS of d) $LaCo_{0.75}Fe_{0.25}O_3$, e) $LaCo_{0.25}Fe_{0.75}O_3$, and f) $LaCoO_3$. g) The site-dependent PDOS of Co-3d in $LaCo_{0.75}Fe_{0.25}O_3$. h) The site-dependent PDOS of Fe-3d in $LaCo_{0.75}Fe_{0.25}O_3$. i) The PDOS of key adsorbates on $LaCo_{0.75}Fe_{0.25}O_3$ during OER.

2.4. Electrochemical behaviors

The pre-oxidation of Co (II) to Co (III) or a higher oxidation state in oxides is considered to be a critical step to generate active CoOOH sites during OER.[27] The per-oxidation behavior of the Co species was investigated by continuous CV cycles (Figure 4a and S20, Supporting Information). The potentials between 1.35−1.52 V vs RHE can be attributed to the $Co^{3+}/^{4+}$ redox couples. The absence of the redox peaks of $Co^{2+}/^{3+}$ indicates that irreversible reconstruction occurs on the surface of the catalysts, evolving a stable catalytic surface for the OER.[28] In addition, we found that the presence of Fe has different effects on the pseudocapacitive behaviours in the process of oxyhydroxide formation. $LaCoO_3$ approached stable states after

two cycles, while the OER activities of $LaCo_{0.75}Fe_{0.25}O_3$ and $LaCo_{0.25}Fe_{0.75}O_3$ gradually increased with the redox peaks being more prominent during successive cycling and their restructured surfaces reached relatively steady states until 100 cycles. As shown in Figure 4b, the anodic peak of the oxidation of Co^{3+} to Co^{4+} in the second cycle for $LaCo_{0.75}Fe_{0.25}O_3$ and $LaCo_{0.25}Fe_{0.75}O_3$ appear at 1.41 V and 1.43 V, respectively, while the anodic peak is observed at higher potentials for $LaCoO_3$ (1.47 V). The results show that the introduction of Fe promotes the oxidation of Co (III), thus facilitating the formation of Co oxyhydroxide species. Figure 4c shows OER CV curves for $LaCo_{1-x}Fe_xO_3$ (x = 0.00, 0.25 and 0.75) in 1.0 M KOH electrolyte. Much better OER activity was found for $LaCo_{0.75}Fe_{0.25}O_3$ than for $LaCo_{0.25}Fe_{0.75}O_3$ and $LaCoO_3$. In particular, $LaCo_{0.75}Fe_{0.25}O_3$ shows a very small overpotential of 310 mV to achieve a current density of 10 mA cm^{-2}, which is much lower than that for $LaCo_{0.25}Fe_{0.75}O_3$ (370 mV) and $LaCoO_3$ (430 mV). Moreover, the reaction kinetics was assessed by the Tafel plots. As seen in the inset of Figure 4c, the Tafel slope for $LaCo_{0.75}Fe_{0.25}O_3$ (58 mV dec^{-1}) is smaller than those for $LaCo_{0.25}Fe_{0.75}O_3$ (75 mV dec^{-1}) and $LaCoO_3$ (89 mV dec^{-1}), implying faster OER rates. To identify the intrinsically catalytic activity of each active site, the specific activity (current per electrochemical active surface area, Figure S21, Supporting Information) of the electrocatalyst for OER was obtained. We normalized the current density to ECSA estimated from double-layer capacitance measurements (Figure S22, Supporting Information). The specific activity of $LaCo_{0.75}Fe_{0.25}O_3$ and $LaCo_{0.25}Fe_{0.75}O_3$ are 0.68 and 0.16 mA cm^{-2} $_{ECSA}$, respectively, which are much higher than that for the pristine $LaCoO_3$ (0.04 mA cm^{-2} $_{ECSA}$), revealing the intrinsic optimization of active sites due to the Fe substitution. Meanwhile, the turnover frequency (TOF) is another crucial parameter reflecting the intrinsic activity of an electrocatalyst.[29] With the introduction of Fe, the TOF of samples was greatly improved with the $LaCo_{0.75}Fe_{0.25}O_3$ being the best (0.27), which is approximately 2.7-fold and 9-fold higher than those of $LaCo_{0.25}Fe_{0.75}O_3$ (0.10) and $LaCoO_3$ (0.03), respectively (Figure 4d). These results demonstrate that Fe substitution has a significant effect on the OER activity. On the other side, the reaction trend of OER is also reflected by the energy change during the process (Figure 4e). For the OER process, both $LaCo_{0.75}Fe_{0.25}O_3$ and $LaCoO_3$ have exhibited the continuous uphill trend under U = 0 V. For the adsorption of OH^-, both electrocatalysts show similar energy change. The largest barrier of the OER occurs at the conversion from O* to OOH*, which shows an energy barrier of 1.47 and 1.76 eV on $LaCo_{0.75}Fe_{0.25}O_3$ and $LaCoO_3$, respectively. The significantly reduced energy barrier for the rate-determining step (RDS) guarantees the high OER performance on $LaCo_{0.75}Fe_{0.25}O_3$. With the applied equilibrium potential (U = 1.23 V), the overpotential of OER has been calculated to be 0.24 V for $LaCo_{0.75}Fe_{0.25}O_3$, which is much smaller than that of

$LaCoO_3$ (Figure 4f). These results have supported that the suitable introduction of Fe improves OER performance due to the optimized electronic structures and stability. Electrochemical impedance spectroscopy (EIS) was performed to investigate the charge-transport properties. The charge-transfer resistance of $LaCo_{0.75}Fe_{0.25}O_3$ (22.58 Ω) was also substantially reduced in comparison to that of $LaCo_{0.25}Fe_{0.75}O_3$ (34.02 Ω) and pristine $LaCoO_3$ (50.92 Ω), suggesting the fast charge-transfer kinetics between electrode and electrolyte during the OER (Figure S23 and Table S5, Supporting Information). Aside from the catalytic activity, long-term operation stability is another critical criterion to evaluate the potential of catalysts for practical application. Remarkably, the $LaCo_{0.75}Fe_{0.25}O_3$ shows excellent durability for 100 hours without obvious degradation. In contrast, $LaCoO_3$ required increased overpotentials to sustain the high current density (Figure S24, Supporting Information). All these results suggest that the $LaCo_{1-x}Fe_xO_3$ (x = 0.00, 0.25 and 0.75) YSNs exhibit excellent performance, compared with corresponding nanoparticles, which can be ascribed to the advantageous structural features of YSNs (Figure S25, Supporting Information). To further identify the origin of YSNs structural advantages, surface hydrophilicity was investigated by contact angle measurements, in which the wetting ability on the electrolyte surface is crucial for electrocatalysis.[30] $LaCo_{0.75}Fe_{0.25}O_3$ YSNs is more hydrophilic with a contact angle of 14.2° (Figure S26, Supporting Information). This excellent superhydrophilicity results in the formation of a wetting film on the surface of the electrode and rapid diffusion of reaction products O_2.

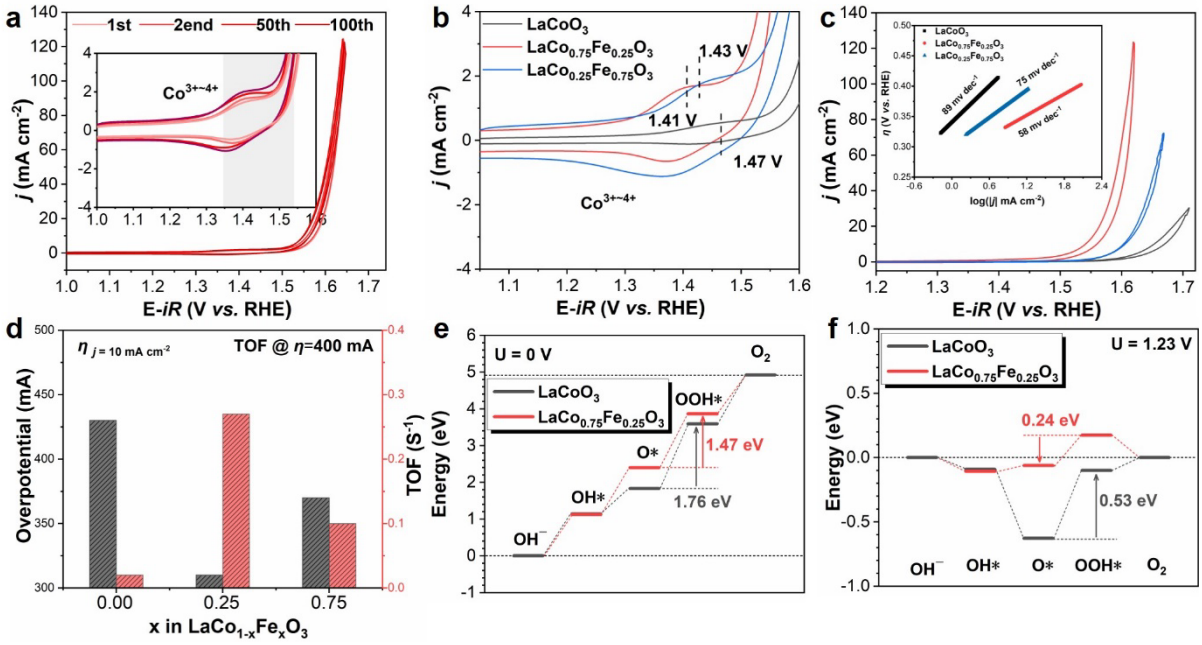

Figure 4. a) CV curves of $LaCo_{0.75}Fe_{0.25}O_3$ measured in 1.0 M KOH at a scan rate of 10 mV s^{-1} for the 1st, 2nd, 50th, and 100th cycles (insets show the capacitive region and the redox waves). b) The capacitive region of the 2nd cycle CV for $LaCoO_3$, $LaCo_{0.75}Fe_{0.25}O_3$ and

$LaCo_{0.25}Fe_{0.75}O_3$. c) OER polarization curves and corresponding Tafel plots of all catalysts. d) The overpotentials at 10 mA cm^{-2} and TOF at 1.63 V. e) The reaction energies of OER under U = 0 V. f) The reaction energies of OER under U = 1.23 V.

2.5. Surface Reconstruction

Hence, in situ Raman spectroscopy was performed to further elucidate the dynamic evolution of those materials during OER (Figure 5a). Two well-defined bands at 557 and 650 cm^{-1} assigned to the bending and stretching vibrations of Co-O can be observed over the samples (Figure 5b).[31] At potentials below 1.45 V_{RHE}, the peak intensities of $LaCo_{0.75}Fe_{0.25}O_3$ decrease with the increase of applied potential, indicating gradual destruction of the surface structure. It clearly shows that CoOOH signal of $LaCo_{0.75}Fe_{0.25}O_3$ was detected at 478 cm^{-1} until the potential reached 1.45 V_{RHE}, and such a potential can be attributed to the Co(III)/Co(IV) oxidation peak (1.35−1.52 V vs RHE). The peak intensity for CoOOH remains constant with the increase of applied voltage, indicating the formation of a stable catalytic species for OER. Moreover, $LaCoO_3$ requires a higher potential to observe CoOOH signals, while $LaCo_{0.25}Fe_{0.75}O_3$ shows unchanged Raman peaks all the time under the same test conditions (Figure S27, Supporting Information).

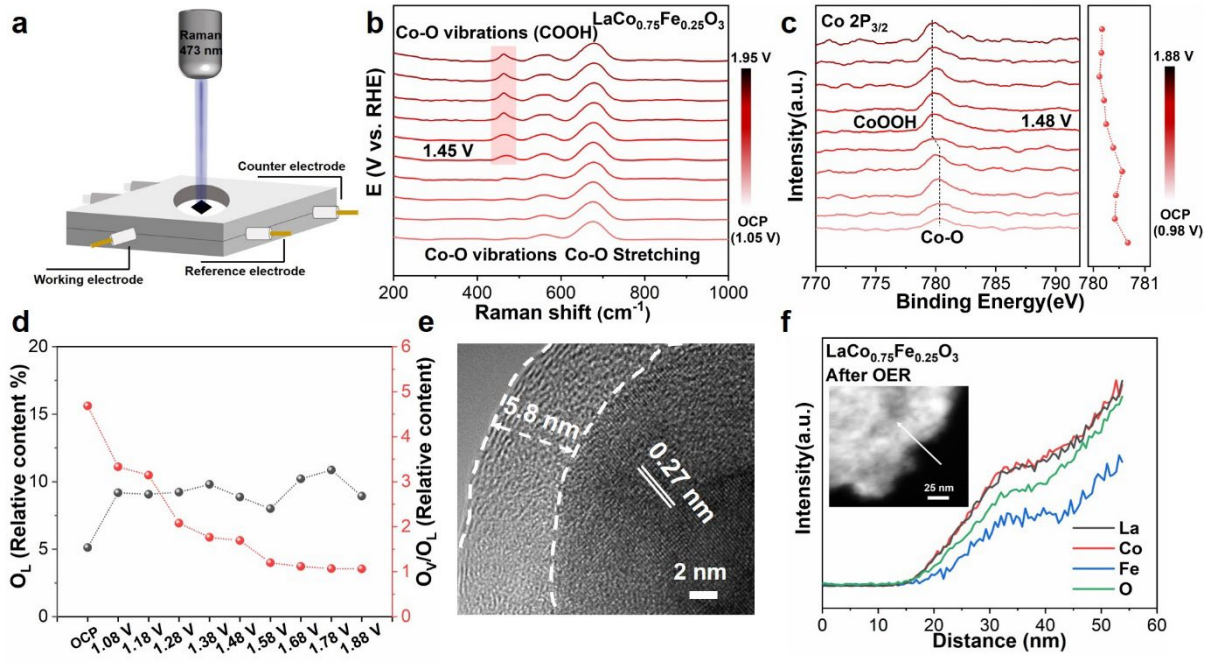

Figure 5. a) The in situ electrochemical Raman cell set-up. b) Potential-dependent in situ Raman spectra of $LaCo_{0.75}Fe_{0.25}O_3$ at 1.05-1.95 V vs RHE with the interval voltage of 100 mV in 1.0 M KOH. c) The *quasi-operando* Co 2p XPS spectra at the applied potential from OCP (0.98 V) to 1.88V vs. RHE in 1.0 M KOH. d) Lattice oxygen relative content and the relative

content of surface oxygen vacancy for $LaCo_{0.75}Fe_{0.25}O_3$. e,f) STEM-EDS image and line scan of $LaCo_{0.75}Fe_{0.25}O_3$ after stability test.

To probe the mechanism of surface reconstruction during OER, the surface structure was analyzed by *quasi-operando* XPS. The signals of the Co-O bonds become weaker and shift towards lower binding energy with the enlarged applied potential, indicating an increase in the relative content and average valence state of Co^{3+}. The peaks of Co-O bonds attributed to CoOOH appear at 781.9 eV when the applied potentials increased to 1.48 V, which is significantly different from the Co-O bonds of perovskites at 780.1 eV. This phenomenon is highly consistent with the pre-oxidation behaviors in situ Raman spectra. However, this potential-dependent reconstruction behavior in pure $LaCoO_3$ is shown slowly and eventually maintained at around 1.68 V, while it is difficult to detect by in situ characterization in $LaCo_{0.25}Fe_{0.75}O_3$ due to the limited reconstruction depth during OER (Figure S28, Supporting Information). Meanwhile, the O_L (lattice oxygen) and the ratio of O_V/O_L (relative content of surface oxygen vacancies) showed an inverse tendency for $LaCo_{0.75}Fe_{0.25}O_3$ during OER. With the increase of applied potential, the relative percentage of lattice oxygen increases from 5.12% to 8.93%, while the ratio of O_V/ O_L decreased rapidly and eventually remains at about 1.06 (Figure 5d and Table S6, Supporting Information). On the contrary, there is almost no significant change trend for $LaCoO_3$ and $LaCo_{0.25}Fe_{0.75}O_3$ (Figure S29, S30 and Table S7, S8, Supporting Information). Therefore, we reasonably conclude that O_V in $LaCo_{0.75}Fe_{0.25}O_3$ is easily filled with OH^- and bonds with cobalt sites, thus forming the active Co-OOH• intermediate of OER.

HRTEM images show that the outermost region of $LaCo_{0.75}Fe_{0.25}O_3$ form an amorphous oxyhydroxide layer with a depth of ~5.8 nm after durability test (Figure 5e), whereas the inner region still maintains the crystalline bulk phases of $LaCo_{0.75}Fe_{0.25}O_3$ as evidenced by the XRD (Figure S31, Supporting Information). A similar phenomenon was observed in $LaCoO_3$ and $LaCo_{0.25}Fe_{0.75}O_3$, but reconstruction depth was limited (Figure S32, Supporting Information). The STEM-EDS further reveals the elemental composition for the restructured surface. The Co and Fe species initially appear on the surface of $LaCo_{0.75}Fe_{0.25}O_3$ in the stoichiometric proportion (3:1) (Figure S33, Supporting Information). The line profile scan shows an abundance of Co distribution in the surface domain (Figure 5f and Figure S34, Supporting Information). Thus, the reconstruction facilitated by Fe substitution is the most critical step in the formation of active surface oxyhydroxide. In contrast, Fe-free $LaCoO_3$ required higher electrochemical potentials to initiate the surface reconstruction.

2.6. Zn–air battery performance evaluation

We have further tested the ORR activities of the electrocatalysts using a rotating ring disk electrode (RRDE) in 0.1 M KOH. The LSV curves demonstrated that the $LaCo_{0.75}Fe_{0.25}O_3$ exhibits the best ORR performance with an onset potential (E_{onset}) of 0.85 V, half-wave potential ($E_{half\text{-}wave}$) of 0.84 V, as well as limiting current of −4.60 mA cm^{-2}, compared with $LaCoO_3$ and $LaCo_{0.25}Fe_{0.75}O_3$ (Figure 6a). To further confirm the electrocatalytic kinetics, the LSV curves at different rotating rates were measured to calculate the number of transferred electrons using Koutecky-Levich plots (K-L) (Figure S35, Supporting Information). The number of transferred electrons of the $LaCo_{0.75}Fe_{0.25}O_3$ was 3.92, which implies its most favorable ORR kinetics via the four-electron pathway. Then the potential differences ($\Delta E = E_{j\,=\,10} - E_{half\text{-}wave}$) between OER potentials at 10 mA cm^{-2} ($E_{j\,=\,10}$) and ORR half-wave potentials ($E_{half\text{-}wave}$) are calculated to directly elucidate the bifunctional activity. $LaCo_{0.75}Fe_{0.25}O_3$ exhibits an outstanding overall electrode performance with the smallest ΔE of 0.90 V (Figure 6b).

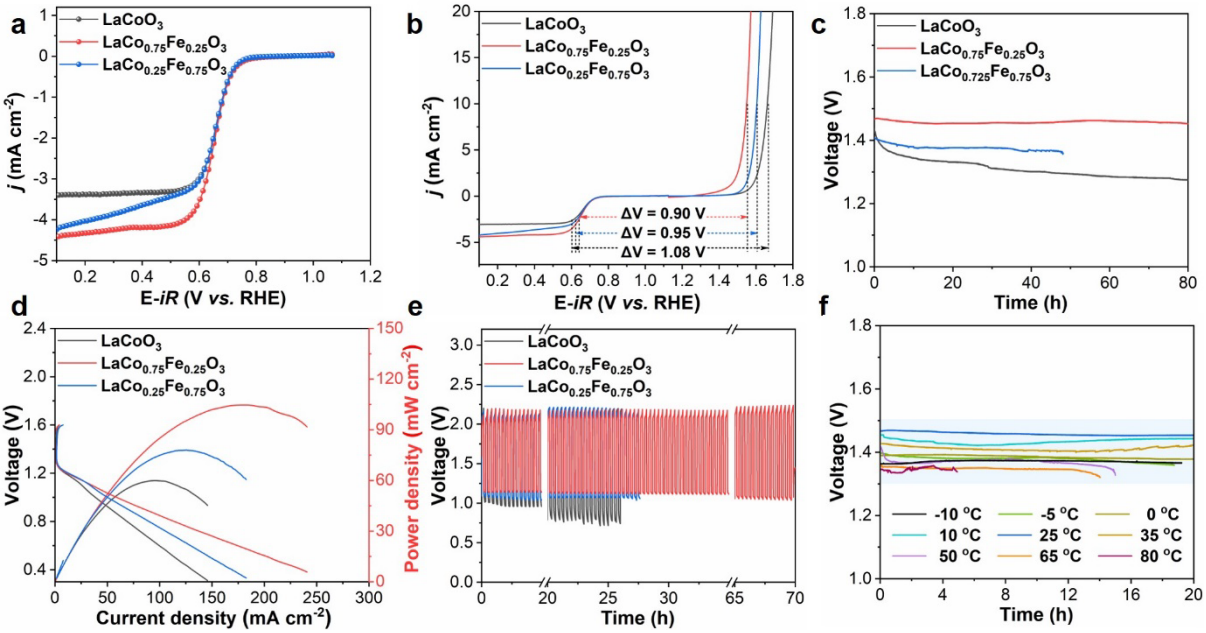

Figure 6. a) ORR polarization curves of $LaCoO_3$, $LaCo_{0.75}Fe_{0.25}O_3$ and $LaCo_{0.25}Fe_{0.75}O_3$. b) Overpotential differences between the $E_{half\text{-}wave}$ of ORR and $E_{j\,=\,10}$ of OER. c) The open-circuit plot. d) The polarization and corresponding power density curves of Zn−air batteries with the for $LaCoO_3$, $LaCo_{0.75}Fe_{0.25}O_3$ and $LaCo_{0.25}Fe_{0.75}O_3$ as air-cathodes, respectively. e) Galvanostatic discharge-charge cycling curves of rechargeable Zn−air batteries. f) The open-circuit plot at different temperatures.

Considering the excellent bifunctional catalytic activity of $LaCo_{0.75}Fe_{0.25}O_3$ for OER and ORR, we assemble an all-solid-state flexible Zn−air battery to further identify its performance under practical operation conditions (Figure S36, Supporting Information). A high open-circuit

voltage of 1.47 V was obtained for a single $LaCo_{0.75}Fe_{0.25}O_3$-based flexible ZAB, and two batteries in series can effectively power different light-emitting diodes (LEDs) under ambient conditions (Figure 6b and Figure S37, Supporting Information). As shown in Figure 6c and 6d, this flexible ZAB exhibits a higher power density of 106 mW cm^{-2} and a cycle life of more than 70 h (up to 300 cycles), demonstrating excellent rechargeability and stability. Notably, it can be found that there is no obvious change in both discharge and charge voltage and this battery is still able to power blue light-emitting diodes when twisted by different angles, which demonstrates its excellent flexibility (Figure S38, Supporting Information). Furthermore, we also explore potential applications in a large temperature range. Figure 6f clearly reveals that the OCV of this flexible ZAB with $LaCo_{0.75}Fe_{0.25}O_3$ as the air-electrode exhibits only small fluctuation even over a large temperature range (-5 ºC to 80 ºC). The specific capacity and duration time decrease almost linearly with the increase or decrease of temperature, and the optimal effect (specific capacity: 842.58 mAh g^{-1}_{Zn} and duration time: 20 h) is achieved when the temperature is 25 ºC (Figure S39, Supporting Information). Additionally, the charge-discharge voltage plateau is maintained very well and long cycle life is realized at different temperatures (Figure S40, Supporting Information). These features demonstrate the decent rechargeability, anti-freezing and heat-resistant properties, and robust stability of the $LaCo_{0.75}Fe_{0.25}O_3$-based flexible battery, conferring its great promise in practical application.

3. Conclusions

In summary, we have developed an efficient and controllable ligand-assisted method to fabriacte the $LaCo_{1-x}Fe_xO_3$ perovskite microspheres with unique yolk-shell structure, which show remarkable electrocatalytic activity and stability toward OER. The rational selection of the ligand is the key for the successful synthesis of perovskite oxide YSNs with controllable component, which shows great potential for other perovskite oxides YSNs to achieve the accurate control of A and B cation ions. Owing to the advantages of the yolk-shell architecture $LaCo_{0.75}Fe_{0.25}O_3$ reaches outstanding electrocatalytic performances induced by the efficient reaction kinetics and mass transports. In addition, the Fe-doping strategy successfully modualtes the electronic structure by optimizeing e_g electron filling and stabilizeing the valence states of Co sites to maintain the high electroactivity, further enhancing electrocatalytic performances. When applied the synthesized $LaCo_{0.75}Fe_{0.25}O_3$ as air cathode, the assembled ZABs demonstrates a large open-circuit voltage of 1.47 V, high energy density of 905 Wh kg^{-1}_{Zn} and stable cyclability of 70 h, together with the excellent mechanical flexibility and potential for operation in a wide temperature window. This work provides an effective strategy for the

design of high-performance perovskite-type electrocatalysts for broad applications in energy conversion and storage devices.

4. Experimental Section

Chemical Materials. Lanthanum(III) nitrate hexahydrate ($La(NO_3)_3·6H_2O$, 99.9%), cobalt(II) nitrate hexahydrate ($Co(NO_3)_2·6H_2O$, 99.0%), iron(III) nitrate nonahydrate ($Fe(NO_3)_3·9H_2O$, 98.5%), nickel(II) nitrate hexahydrate ($Ni(NO_3)_2·6H_2O$, 98.0%), cerium(III) nitrate hexahydrate ($Ce(NO_3)_3·6H_2O$, 99.5%), 1,3,5-Benzenetricarboxylic acid (1,3,5-BTC, 99.0%), potassium hydroxide (KOH, 99.9%), *N*,*N*-dimethylacetamide (DMAC, 99.8%), ethanol (EtOH, 99.5%) and Nafion (5 wt%) were purchased from Aladdin. The commercial carbon fiber papers (CFP) was purchased from Fuel Cell Store. The demonized (DI) water was obtained from a Millipore Autopure system (18.2 MΩ, Millipore Ltd., USA). All the other materials for electrochemical measurements were analytical grade and can be used without further purification.

Synthesis of $LaCo_{1-x}Fe_xO_3$ YSNs: The stoichiometric amounts of $La(NO_3)_3·6H_2O$ (0.5 mmol) and $Co(NO_3)_2·6H_2O$ (0.5 mmol) were dissolved in DMAC (60 mL) and stirred for 15 min to form a clear solution. Then 1,3,5-BTC (1.2 mmol) was added into the above solution and stirring for more than 1 h. After that the solution was transferred to a 100 mL Teflon-lined stainless-steel autoclave and maintained at 130 ºC for 10 h. The suspension was centrifuged at 7000 rpm for 5 min and washed with ethanol for several times. The obtained products were dried at 70 ºC for 2 h and annealed at 650 ºC (2 °C/min) in air for 5 h to get the $LaCoO_3$ YSNs. The synthesis of $LaCo_{1-x}Fe_xO_3$ YSNs (x = 0.10, 0.25, 0.75 and 1.00) were similar to that of $LaCoO_3$ except using different molar ratios of Co:Fe at the beginning. A similar procedure was also adopted to prepare $LaCo_{0.75}Ni_{0.25}O_3$ and $La_{0.9}Ce_{0.1}CoO_3$ YSNs.

Synthesis of $LaCo_{1-x}Fe_xO_3$ NPs: $LaCo_{1-x}Fe_xO_3$ NPs were prepared through a sol-gel method. In a typical synthesis, stoichiometric amounts of $La(NO_3)_3·6H_2O$ (3.75 mmol), $Co(NO_3)_2·6H_2O$ (3.75 mmol) and urea (15.0 mmol) were dissolved in a mixture solution of deionized water (30 mL) and nitric acid (3 mL) to obtain a homogeneous solution, followed by the addition of citric acid (15.0 mmol). Then the above solution was heated at 80 °C under stirring until a gel generated and further dried at 180 °C for 12 h. The precursor powders were further annealed at 650 °C for 6 h in air to produce $LaCoO_3$ NPs. The $LaCo_{1-x}Fe_xO_3$ (x = 0.25 and 0.75) were also prepared by using $Fe(NO_3)_3·9H_2O$ to substitute $Co(NO_3)_2·6H_2O$ with equal molar amount.

Synthesis of hydrogel: To make the solid electrolyte, polyvinyl alcohol (PVA, MW 195000, 4.0 g) was firstly dissolved in deionized water (40 mL) at 95 °C under magnetic stirring for 2 h to form a uniform gel. Then KOH (4 mL, 18 M) solution was added and the electrolyte solution was kept stirring at 95 °C for 40 min. Finally, the solution was transferred to the container and keep in a refrigerator for 4 h.[32]

Physicochemical Characterizations: X-ray diffraction (XRD) measurements were carried out on Rigaku MiniFlex 600 diffractometer with Cu Kα radiation (λ = 0.1542 nm) from 10° to 90° under a voltage of 40 kV. Scanning electron microscopy (SEM) images and energy dispersive X-ray spectroscopy (EDS) were taken with a ThermoFisher Apreo S filed-emission scanning electron microscopy (FE-SEM) at an acceleration voltage of 30 kV. Transmission electron microscopy (TEM) and high-resolution transmission electron microscopy (HRTEM) images were obtained on a Tecnai G2 F30 Field Emission Transmission Electron Microscope. Atomic-scale STEM images were recorded on a probe aberration-corrected STEM (Cubed Titan G2 60-300, FEI, USA) operated at 300 kV. X-ray photoelectron spectroscopy (XPS) analysis was made with a Kratos Axis Supra device and corrected with C 1s line at 284.8 eV. Sample compositions was measured by inductively coupled plasma optical emission spectrometry (ICP-OES) using a Plasma Quant PQ9000 ICP spectrometer. The contact angle measurements were carried out on a Kruss DSA100 optical contact angle/surface tension meter. The magnetization measurements were carried out with a Superconducting Quantum Interference Device (SQUID, Quantum Design). The Raman spectroscopy measurements were conducted on an LabRAM HR Evolution spectrophotometer with 473 nm wavenumber of the excitation light source. Synchrotron radiation X-ray absorption fine structure (XAFS) spectroscopy at the Co, Fe and O K-edge were collected in transmission mode using a Si (111) double-crystal monochromator at the 1W1B station of the Beijing Synchrotron Radiation Facility (BSRF).

Electrochemical measurements: Electrochemical tests were performed in 1.0 and 0.1 M KOH solutions with a standard three-electrode setup at room temperature on the CHI-760E Electrochemical Workstation (CHI Instruments, Shanghai Chenhua Instrument Corp., China). Saturated Hg/HgO and Pt plate were used as the reference and the counter electrodes, respectively. The working electrode was the catalyst-loaded glassy carbon electrode (GC, 0.071 cm^2) or a rotating ring-disk electrode (RRDE, 0.096 cm^2). To prepare the working electrode, electrocatalyst (8.0 mg), carbon black (2.0 mg) and Nafion perfluorinated resin solution (40 μL, 5 wt.%) were dispersed in a mixed solution of deionized water (3.2 mL) and isopropanol (0.8 mL), followed by ultrasonication for at least 30 min to form a mixed ink. Then this solution (7.1 μL) was dropped on the polished GC electrode and dried naturally, generating a catalyst

loading of 0.2 mg cm^{-2}. For ORR, the above ink (19.6 μL) should be drop-casted onto the RRDE to achieve the same load. The measured potentials were converted to a reversible hydrogen electrode (RHE) through the Nernst equation ($E_{RHE} = E_{Hg/HgO} + 0.0951pH + 0.098$ and $E_{RHE} = E_{Ag/AgCl} + 0.0591pH + 0.197$). Additionally, the *iR*-compensation with 90% for the linear sweep voltammetry (LSV) curves were made by CHI 760 E software. The Raman measurements were investigated using the in situ electrochemical Raman cell (031-2H) with a saturated Ag/AgCl reference electrode and a Pt ring counter electrode. Potential-dependent in situ Raman spectra and quasi-operando XPS tests were carried out in 1.0 M KOH with an interval time of 10 min to detect the surface chemical composition and structural evolution of materials.

Zn−air battery assembly and measurements: The solid-state Zn−air battery was assembled with polished Zn foil (2 × 1 cm) as the anode, and the carbon fiber paper (CFP, 2 × 1 cm) coated with catalysts (mass loading of 2 mg cm^{-2}) as the air cathode and polyvinyl alcohol (PVA) glue as the electrolyte. The polarization curves were performed by LSV at a scan rate of 5 mV s^{-1} using CHI 760E electrochemical workstation. The galvanostatic charge-discharge curves were recorded using a LAND CT 2001A multi-channel battery testing system. The ZABs were tested under different temperatures by the temperature-controlled equipment (BTC−405, −40~130 ºC).

Calculation Setup: To study the effect of Fe doping in $LaCoO_3$ perovskite for the OER, DFT calculations have been applied to investigate the electronic structures and reaction trends through the CASTEP codes.[33] We have selected the generalized gradient approximation (GGA) with Perdew-Burke-Ernzerhof (PBE) as the key functionals to describe the exchange-correlation energy.[34–36] The plane-wave basis cutoff energy has been set to 380 eV and the ultrasoft pseudopotentials have been chosen for all the geometry optimizations. The Broyden-Fletcher-Goldfarb-Shannon (BFGS) algorithm has been applied and we select the coarse quality of k-points for all the energy minimizations based on the balance between calculation precision and loading.[37] As the experimental characterizations, we have constructed three different electrocatalyst surfaces including $LaCoO_3$, $LaCo_{0.75}Fe_{0.25}O_3$ and $LaCo_{0.25}Fe_{0.75}O_3$ to observe the influences of Fe doping. All the models have been cleaved with the (110) surfaces with six-layer thickness. To guarantee full relaxation, we introduce a vacuum space of 20 Å in the z-axis of the model. Most importantly, to reach the geometry optimizations, we have set the following convergence criteria for all the calculations, including the Hellmann-Feynman forces on the atom should not exceed 0.001 eV/Å, the total energy difference and the inter-ionic displacement should be less than 5×10^{-5} eV/atom and 0.005 Å, respectively.

Acknowledgements

We acknowledge support from the National Natural Science Foundation of China (No. 21922105 and 21931001), the National Key R&D Program of China (2021YFA1501101), the Special Fund Project of Guiding Scientific and Technological Innovation Development of Gansu Province (2019ZX-04) and the 111 Project (B20027). We also acknowledge support by the Fundamental Research Funds for the Central Universities (lzujbky-2021-pd04, lzujbky-2021-it12 and lzujbky-2021-37). B.H. acknowledges the support of the Natural Science Foundation of China/RGC Joint Research Scheme (No. N_PolyU502/21), and the funding for Projects of Strategic Importance of the Hong Kong Polytechnic University (Project No. 1-ZE2V)

References:

[1] D. Larcher, J.-M. Tarascon, *Nat. Chem.* **2015**, *7*, 19.

[2] J. Fu, Z. P. Cano, M. G. Park, A. Yu, M. Fowler, Z. Chen, *Adv. Mater.* **2017**, *29*, 1604685.

[3] J. Yin, Y. Li, F. Lv, M. Lu, K. Sun, W. Wang, L. Wang, F. Cheng, Y. Li, P. Xi, S. Guo, *Adv. Mater.* **2017**, *29*, 1704681.

[4] J. Yu, B. Li, C. Zhao, J. Liu, Q. Zhang, *Adv. Mater*. **2020**, *32*, 1908488.

[5] Q. Liu, Z. Chang, Z. Li, X. Zhang, *Small Methods*. **2018**, *2*, 1700231.

[6] H.-F. Wang, C. Tang, Q. Zhang, *Adv. Funct. Mater.* **2018**, *28*, 1803329.

[7] J. Song, C. Wei, Z.-F. Huang, C. Liu, L. Zeng, X. Wang, Z. J. Xu, *Chem. Soc. Rev.* **2020**, *49*, 2196.

[8] J. Suntivich, H. A. Gasteiger, N. Yabuuchi, H. Nakanishi, J. B. Goodenough, Y. Shao-Horn, *Nat. Chem.* **2011**, *3*, 546.

[9] J. Hwang, R. R. Rao, L. Giordano, Y. Katayama, Y. Yu, Y. Shao-Horn, *Science* **2017**, *358*, 751.

[10] W. Wang, M. Xu, X. Xu, W. Zhou, Z. Shao, *Angew. Chem., Int. Ed.* **2020**, *59*, 136.

[11] Z. Zeng, Y. Xu, Z. Zhang, Z. Gao, M. Luo, Z. Yin, C. Zhang, J. Xu, B. Huang, F. Luo, Y. Du, C. Yan, *Chem. Soc. Rev.* **2020**, *49*, 1109.

[12] X. Cheng, E. Fabbri, M. Nachtegaal, I. E. Castelli, M. E. Kazzi, R. Haumont, N. Marzari, T. J. Schmidt, *Chem. Mater.* **2015**, *27*, 7662.

[13] Y. Zhu, W. Zhou, Y. Che, J. Yu, M. Liu, Z. Shao, *Adv. Mater.* **2015**, *27*, 7150.

[14] J. Suntivich, K. J. May, H. A. Gasteiger, J. B. Goodenough, Y. Shao-Horn, Science *2011*, **334**,1383.

[15] A. Grimaud, O. D. Morales, B. Han, W. T. Hong, Y. L. Lee, L. Giordano, K. A. Stoerzinger, M. T. M. Koper, Y. Shao-Horn, *Nat. Chem*. **2017**, *9*, 457.

[16] J. Liu, S. Qiao, J. Chen, X. W. Lou, X. Xing, G. Lu, *Chem. Commun.* **2011**, *47*, 12578.

[17] L. Zhou, H. Xu, H. Zhang, J. Yang, S. B. Hartono, K. Qian, J. Zou, C. Yu, *Chem. Commun.* **2013**, *49*, 8695.

[18] L. Xu, Q. Jiang, Z. Xiao, X. Li, J. Huo, S. Wang, L Dai, *Angew. Chem. Int. Ed.* **2016**, *55*, 5277.

[19] L. Zhuang, L. Ge, Y. Yang, M. Li, YJia, X. Yao, Z. Zhu, *Adv. Mater.* **2017**, *29*, 1606793.

[20] D Chen, M. Qiao, Y. R. Lu, L. Hao, D. Liu, C. L. Dong, Y. Li, S. Wang, *Angew. Chem. Int. Ed.* **2018**, *57*, 8691.

[21] S. K. Pandey, S. Khalid, N. P. Lalla, A. V. Pimpale, *J. Phys.: Condens. Matter* **2006**, *18*, 10617.

[22] Y. Tong, Y. Guo, P. Chen, H. Liu, M. Zhang, L. Zhang, W. Yan, W. Chu, C. Wu, Y. Xie, *Chem* **2017**, *3*, 812.

[23] O. Toulemonde, N. N. Guyen, F. Studer, *J. Solid State Chem.* **2001**, *158*, 208.

[24] M. Merz, P. Nagel, C. Pinta, A. Samartsev, H. V. Lohneysen, M. Wissinger, S. Uebe, A. Assmann, D. Fuchs, S. Schuppler, *Phys. Rev. B*. **2010**, *82*, 174416.

[25] R. F. Klie, J. C. Zheng, Y. Zhu, M. Varela, J. Wu, and C. Leighton, *Phys. Rev. Lett*. 2007,*99*, 047203.

[26] S. Zhou, X. Miao, X. Zhao, C. Ma, Y. Qiu, Z. Hu, J. Zhao, L. Shi, J. Zeng, *Nat. Commun.* **2016**, *7*, 11510.

[27] B. S. Yeo, A.T. Bell, *J. Am. Chem. Soc.* **2011**, *133*, 5587.

[28] K. J. May, C. E. Carlton, K. A. Stoerzinger, M. Risch, J. Suntivich, Y.-L. Lee, A. Grimaud, Y. Shao-Horn, *J. Phys. Chem. Lett.* **2012**, *3*, 3264.

[29] J. Kibsgaard, T. F. Jaramillo, *Angew. Chem. Int. Ed.* **2014**, *53*, 14433.

[30] H. Li, S. Chen, Y. Zhang, Q. Zhang, X. Jia, Q. Zhang, L. Gu, X. Sun, L. Song, X. Wang, *Nat. Commun.* **2018**, *9*, 2452.

[31] N. Orlovskaya, D. Steinmetz, S. Yarmolenko, D. Pai, J. Sankar, J. Goodenough, *Phys. Rev. B*. 2005, *72*, 014122.

[32] F. Meng, H. Zhong, D. Bao, J. Yan, X. Zhang, *J. Am. Chem. Soc.* **2016**, *138*, 10226.

[33] S. J. Clark, M. D. Segall, C. J. Pickard, P. J. Hasnip, M. I. J. Probert, K. Refson, M. C. Payne, *Z. Kristallogr. Cryst. Mater.* **2005**, *220*, 567.

[34] J. P. Perdew, K. Burke, M. Ernzerhof, *Phys. Rev. Lett.* **1996**, *77*, 3865.

[35] P. J. Hasnip, C. J. Pickard, *Comput. Phys. Commun.* **2006**, *174*, 24.

[36] J. P. Perdew, J. A. Chevary, S. H. Vosko, K. A. Jackson, M. R. Pederson, D. J. Singh, C. Fiolhais, *Phys. Rev. B* **1992**, *46*, 6671.

[37] J. D. Head, M. C. Zerner, *Chem. Phys. Lett.* **1985**, *122*, 264.

Table of contents.

The general ligand-assisted strategy of constructing the yolk-shell nanostructures is achieved for a series of perovskite oxides $LaCo_{1-x}Fe_xO_3$. Structural optimization at the micrometer level and electronic modulation at the atomic level boost the OER performance of $LaCo_{0.75}Fe_{0.25}O_3$.